

pubs.acs.org/JACS Article

# Amorphous Oxyhalide Matters for Achieving Lithium Superionic Conduction

- 3 Shumin Zhang, ◆ Feipeng Zhao, ◆ Lo-Yueh Chang, Yu-Chun Chuang, Zhen Zhang, Yuanming Zhu,
- <sup>4</sup> Xiaoge Hao, Jiamin Fu, Jiatang Chen, Jing Luo, Minsi Li, Yingjie Gao, Yining Huang, Tsun-Kong Sham,
- 5 M. Danny Gu,\* Yuanpeng Zhang,\* Graham King,\* and Xueliang Sun\*



Cite This: https://doi.org/10.1021/jacs.3c07343



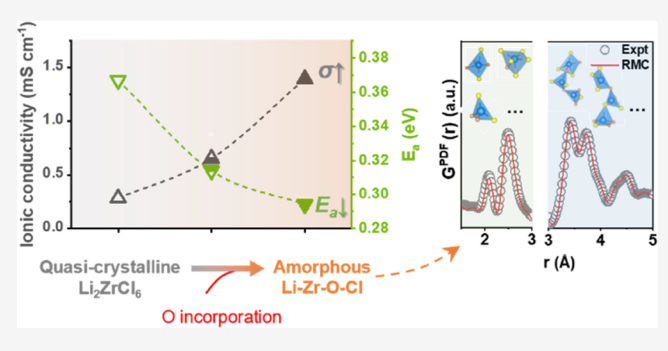
**ACCESS** 

III Metrics & More

Article Recommendations

Supporting Information

6 ABSTRACT: The recently surged halide-based solid electrolytes 7 (SEs) are great candidates for high-performance all-solid-state 8 batteries (ASSBs), due to their decent ionic conductivity, wide 9 electrochemical stability window, and good compatibility with 10 high-voltage oxide cathodes. In contrast to the crystalline phases in 11 halide SEs, amorphous components are rarely understood but play 12 an important role in Li-ion conduction. Here, we reveal that the 13 presence of an amorphous component is common in halide-based 14 SEs that are prepared via mechanochemical synthesis. The fast Li-15 ion migration is found to be associated with the local chemistry of 16 the amorphous proportion. Taking Zr-based halide SEs as an 17 example, the amorphization process can be regulated by



18 incorporating O, resulting in the formation of corner-sharing Zr–O/Cl polyhedrons. This structural configuration has been 19 confirmed through X-ray absorption spectroscopy, pair distribution function analyses, and Reverse Monte Carlo modeling. The 20 unique structure significantly reduces the energy barriers for Li-ion transport. As a result, an enhanced ionic conductivity of  $(1.35 \pm 21\ 0.07) \times 10^{-3}\ S\ cm^{-1}$  at 25 °C can be achieved for amorphous  $\text{Li}_3\text{ZrCl}_4\text{O}_{1.5}$ . In addition to the improved ionic conductivity, 22 amorphization of Zr-based halide SEs via incorporation of O leads to good mechanical deformability and promising electrochemical 23 performance. These findings provide deep insights into the rational design of desirable halide SEs for high-performance ASSBs.

# 1. INTRODUCTION

Green mobility plays a crucial role in achieving the objectives of the clean energy revolution. The transition to electric vehicles heavily depends on the development of advanced battery technologies and efficient production capabilities. 1-3 All-solid-state batteries (ASSBs) with solid electrolytes (SEs) and potentially employing alkaline metal anodes and high-30 voltage cathodes are believed to provide an opportunity for achieving excellent safety and high-energy density. 4-6 In ASSBs, SEs are in direct contact with electrode materials, replacing the flammable organic liquid electrolytes and inert separators. The advancement of SEs governs the development of ASSBs. 7-10

Among different categories of SEs (e.g., oxides, sulfides, 37 hydrides, polymers, hybrids, etc.), halide-based SEs have drawn 38 increasing attention due to their high ionic conductivities (up 39 to  $10^{-2}$  S cm<sup>-1</sup>), good antioxidation stability (over 4 V vs Li<sup>+</sup>/40 Li), and decent mechanical deformability. Since Pana-41 sonic reported Li<sub>3</sub>YCl<sub>6</sub> and Li<sub>3</sub>YBr<sub>6</sub> in 2018, since Pana-42 halides (Li-M-X, M = metal cation, X = halogen anion) have 43 been widely reported. Most ternary halide-based SEs are 44 in crystalline phases, which show either hexagonal-close-45 packed (*hcp*) or cubic-close-packed (*ccp*) anion sublattices. 10

High crystallinity is generally pursued to ensure good ionic 46 conductivity of *ccp* structured SEs, such as representative 47 Li<sub>3</sub>YBr<sub>6</sub>, <sup>15</sup> Li<sub>3</sub>InCl<sub>6</sub>, <sup>16,21</sup> Li–Sc–Cl, <sup>17,22</sup> etc. A ball milling 48 (BM) plus post-annealing or co-melting process contributes to 49 form high-crystalline (*hc*) phases with the optimized ionic 50 conductivity. However, for some halides, such as Li<sub>3</sub>YCl<sub>6</sub>, <sup>15</sup> 51 Li<sub>3</sub>ErCl<sub>6</sub>, <sup>23</sup> and Li<sub>2</sub>ZrCl<sub>6</sub>, <sup>24,25</sup> their low-crystalline (*lc*) phases 52 from a mechanochemical (e.g., high-energy BM) process 53 possess decent ionic conductivities in the order of 10<sup>-4</sup> S cm<sup>-1</sup>, 54 while a post-annealing treatment reduces the ionic conductivity 55 (under the circumstance of maintaining the same crystalline 56 phase). Possible explanations, such as cation sites disorder <sup>23,26</sup> 57 and stacking faults <sup>27</sup> have been proposed. Nevertheless, these 58 understandings based on crystallography knowledge are 59 inadequate to cover all the behaviors of halide SEs synthesized 60 by the one-step mechanochemical method. Discussions about 61

Received: July 10, 2023 Revised: January 6, 2024 Accepted: January 9, 2024



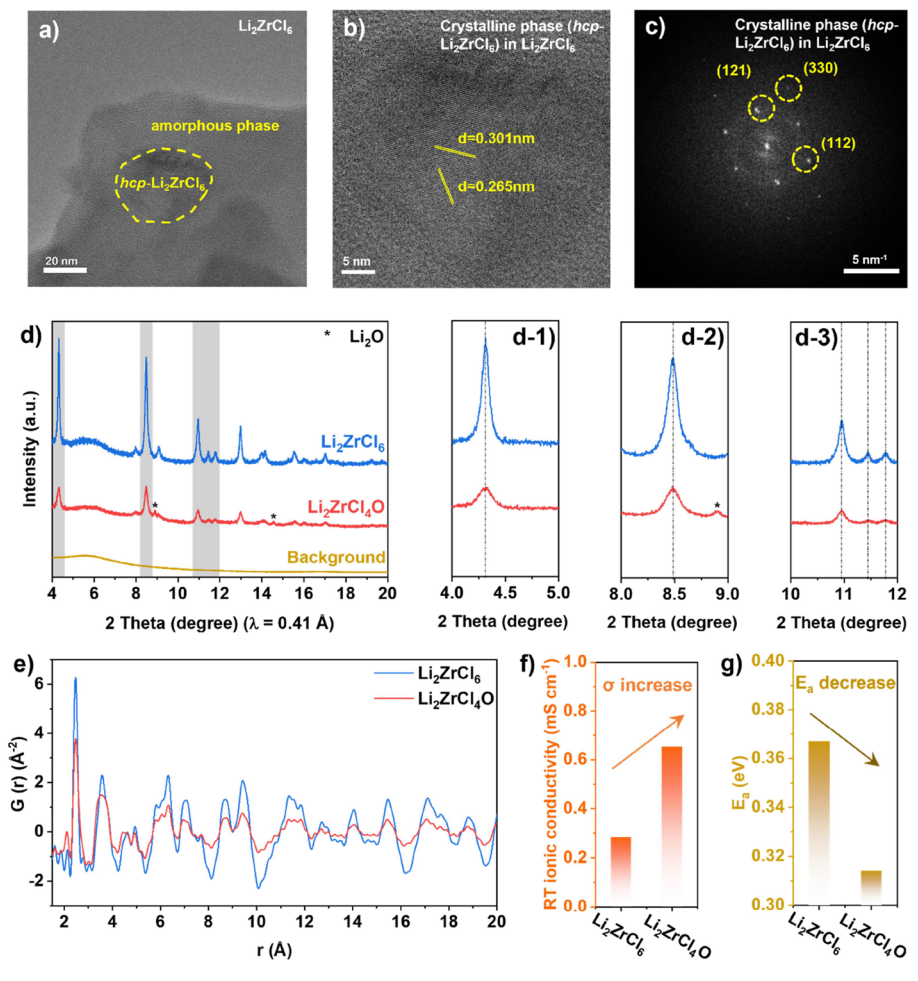


Figure 1. (a) Representative cryo-TEM images of the Li<sub>2</sub>ZrCl<sub>6</sub> with (b, c) its crystalline component (hcp-Li<sub>2</sub>ZrCl<sub>6</sub>). (d) SXRD patterns of the Li<sub>2</sub>ZrCl<sub>6</sub> and Li<sub>2</sub>ZrCl<sub>4</sub>O powders with magnified regions of (d-1) 4–5°, (d-2) 8–9°, and (d-3) 10–12°. Background signal comes from the quartz capillary that we used during the test. (e) Comparison of PDF ( $\lambda \approx 0.23 \text{ Å}$ ) patterns for Li<sub>2</sub>ZrCl<sub>6</sub> and Li<sub>2</sub>ZrCl<sub>4</sub>O materials. Comparisons of (f) ionic conductivities (RT is 25 °C) and (g) activation energies for Li<sub>2</sub>ZrCl<sub>6</sub> and Li<sub>2</sub>ZrCl<sub>4</sub>O SEs.

62 the non-negligible amorphous proportion in the obtained 63 halide SEs $^{28}$  are usually omitted. Wang et al. found the 64 existence of a significant amount of nonperiodic components 65 in  $\text{Li}_2\text{ZrCl}_6$  halide SEs and speculated that the decent ionic 66 conductivity of  $\text{Li}_2\text{ZrCl}_6$  was originated from this nonperiodic 67 structure rather than the specific crystalline phase(s).

Indeed, very recently, amorphous halide SEs have gradually attracted attention. Ishiguro et al. reported an amorphous  $^{70}$  LiTaCl $_6$  SE by using a long-duration (>120 h) BM process,  $^{29}$  which shows excellent ionic conductivity of over  $10^{-2}$  S cm $^{-1}$ . Our group reported a series of amorphous Li-M-O-Cl (M =  $^{73}$  Ta, Hf) oxychloride SEs via constructing mixed-anion (Cl and O) frameworks. The highly disordered M-O/Cl arrangements with corner-sharing of the O and rich terminal Cl are regarded as the main reasons for the fast Li-ion transport (up to  $6.6 \times 10^{-3}$  S cm $^{-1}$  at 25 °C). Although these reported amorphous halide SEs appear promising, either careful regulation of crystalline-to-amorphous transition, or the relevance between the structure and ionic conduction was rarely established. Nevertheless, solving these issues is essential to realize controllable synthesis of desirable halide SEs.

83 In this work, taking the cost-effective Zr-based halide SEs as 84 an example, we first reveal the quasi-amorphous nature of the 85 Li<sub>2</sub>ZrCl<sub>6</sub> synthesized from a typical BM method. Through O 86 incorporation, we further manipulate the amorphization of the Zr-based halide SEs (amorphous content: 69.1-89.5%), 87 understanding the correlation between the enhanced ionic 88 conduction and amorphous component. As a result, an 89 optimized Li<sub>3</sub>ZrCl<sub>4</sub>O<sub>1.5</sub> amorphous SE shows a high ionic 90 conductivity of  $(1.35 \pm 0.07) \times 10^{-3}$  S cm<sup>-1</sup> at 25 °C, which is 91 an order of magnitude increase compared to the quasi- 92 amorphous Li<sub>2</sub>ZrCl<sub>6</sub> ( $10^{-4}$  S cm<sup>-1</sup> level). The structure of 93 Li<sub>3</sub>ZrCl<sub>4</sub>O<sub>1.5</sub> amorphous SE is investigated in depth. 94 Particularly, the combined synchrotron-based spectroscopy 95 and Reverse Monte Carlo (RMC) modeling analyses 96 contribute to disclose the amorphous local structure and its 97 close correlation to the high ionic conductivity. Finally, the 98 practicality of the regulated amorphous Zr-based halide SEs is 99 demonstrated in high-performance ASSBs with conventional 100 layered oxide cathode materials.

## 2. RESULTS AND DISCUSSION

The base material,  $\text{Li}_2\text{ZrCl}_6$ , was synthesized via a BM process 102 (see experimental section for details). As shown in Figure S1, 103 the synchrotron-based X-ray diffraction (SXRD) pattern of the 104 as-prepared  $\text{Li}_2\text{ZrCl}_6$  can be indexed to a trigonal phase with 105 an hcp anionic sublattice. Broad diffraction peaks were 106 observed. This phenomenon also occurs to some other halide 107 SEs prepared by the one-step BM method, such as  $\text{Li}_3\text{YCl}_6$  and 108  $\text{Li}_3\text{ErCl}_6$ . Figure 1a—c shows the cryogenic transition 109 fi

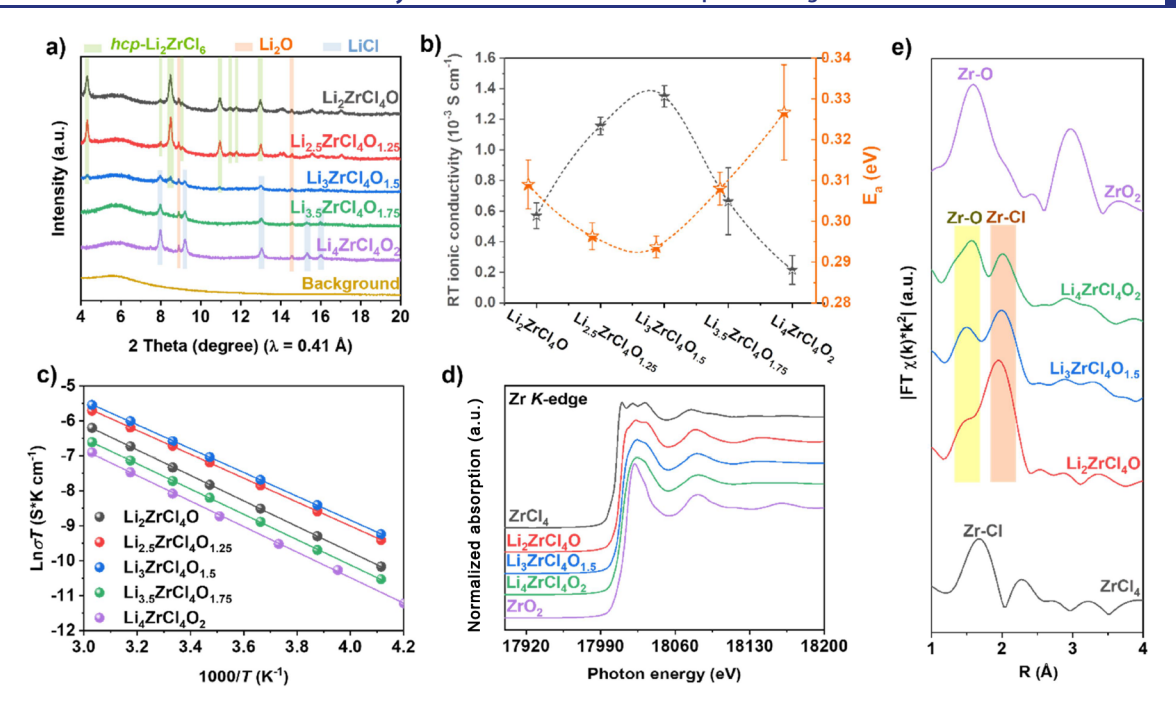


Figure 2. (a) SXRD patterns of the  $\text{Li}_{2+2x}\text{ZrCl}_4\text{O}_{1+x}$  SEs (x = 0, 0.25, 0.5, 0.75, and 1). (b) Comparison of ionic conductivities and activation energies of the  $\text{Li}_{2+2x}\text{ZrCl}_4\text{O}_{1+x}$  SEs. (c) Arrhenius plots of the  $\text{Li}_{2+2x}\text{ZrCl}_4\text{O}_{1+x}$  SEs. (d) XANES and (e) FT-EXAFS spectra of the  $\text{Li}_2\text{ZrCl}_4\text{O}$ ,  $\text{Li}_3\text{ZrCl}_4\text{O}_{1-x}$ , and  $\text{Li}_4\text{ZrCl}_4\text{O}_2$  SEs at the Zr K-edge, respectively. ZrCl<sub>4</sub> and ZrO<sub>2</sub> are reference samples.

110 electron microscopy (cryo-TEM) characterizations of the 111 Li<sub>2</sub>ZrCl<sub>6</sub> powder. Crystalline hcp-Li<sub>2</sub>ZrCl<sub>6</sub> grains were 112 embedded in highly disordered regions. The amorphous 113 proportion may be originated from the mechanochemical 114 synthesis method, in which mechanical energy is transformed 115 into pulverization chemical energy to "thermal quench" the 116 powder samples locally and rapidly with the formation of 117 amorphous regions.<sup>31</sup> In the present study, we used the 118 internal standard method to figure out that the amorphous 119 content in the  $\text{Li}_2\text{ZrCl}_6$  SE was 46.0% (Figure S2), which was 120 similar to the previous report (~48%). As we previously 121 reported superionic amorphous Li-M-O-Cl (M = Ta, Hf) 122 halide SEs,<sup>30</sup> here we further utilize the mixed-anion strategy 123 with systematic O introduction to regulate the amorphization 124 degree of the Zr-based halide SEs and to study the relationship 125 with their ionic conduction. For a base formula of Li<sub>2</sub>ZrCl<sub>6</sub>, 126 partial substitution of Cl by O was achieved by using Li<sub>2</sub>O in 127 place of the LiCl starting material while maintaining the Li/Zr 128 molar ratio of 2:1. The resultant Li<sub>2</sub>ZrCl<sub>4</sub>O exhibited a similar 129 diffraction pattern to that of Li<sub>2</sub>ZrCl<sub>6</sub> except for a small 130 amount of residual Li<sub>2</sub>O (Figure 1d). Comparing Li<sub>2</sub>ZrCl<sub>4</sub>O to 131 Li<sub>2</sub>ZrCl<sub>6</sub>, theoretically, a considerable amount of the Cl was 132 replaced by O (33.3%), which showed a higher O substitution  $_{133}$  percentage compared to previous reports about doping O (8–  $_{134}$  21%) in the  $\rm Li_2ZrCl_6$  SEs,  $^{32-34}$  demonstrating a robust 135 inclusive capability of our synthesis route. Nevertheless, 136 although there is a big difference in radius between Cl<sup>-</sup> (181 137 pm) and O<sup>2-</sup> (140 pm), a nonobservable peak shift appeared 138 in the Li<sub>2</sub>ZrCl<sub>4</sub>O SE (see the magnified regions from Figure 139 1d-1-d-3). This indicated that O was not doped into the 140 structure of crystalline hcp-Li<sub>2</sub>ZrCl<sub>6</sub> but altered the properties 141 of the amorphous phase that increased to 69.1% in Li<sub>2</sub>ZrCl<sub>4</sub>O 142 SE. The incorporation of the O into the amorphous portion of 143 the Li<sub>2</sub>ZrCl<sub>4</sub>O SE was further verified by conducting electron 144 energy loss spectroscopy (EELS) element mapping as 145 displayed in Figure S3.

Figure 1e shows the pair distribution function (PDF) 146 profiles of Li<sub>2</sub>ZrCl<sub>6</sub> and Li<sub>2</sub>ZrCl<sub>4</sub>O materials. Compared with 147 Li<sub>2</sub>ZrCl<sub>6</sub>, the reduced peak intensity and widened peak width 148 for Li<sub>2</sub>ZrCl<sub>4</sub>O suggested a higher amorphous content with 149 disordered structures inside. Furthermore, combined with 150 wavelet-transformed (WT) extended x-ray absorption fine 151 structure (EXAFS) and Fourier-transformed (FT) EXAFS 152 fitting results (Figure S4 and Table S1), an emerged peak at 153 2.09 Å in the Li<sub>2</sub>ZrCl<sub>4</sub>O PDF profile can be attributed by Zr- 154 O bonding. An asymmetric peak between 3 and 4 Å 155 corresponds to connection diversity between Zr-centered 156 polyhedrons. More importantly, the dominance of the 157 amorphous content in the Li<sub>2</sub>ZrCl<sub>4</sub>O sample can be verified 158 by measuring the ionic conductivity and activation energy 159 (Figure S5). As displayed in Figure 1f,g, after tuning and 160 increasing the amorphous content via O participation with the 161 formation of Li<sub>2</sub>ZrCl<sub>4</sub>O, there was a double increase in the 162 ionic conductivity (at 25 °C), accompanied with a decreased 163 activation energy.

We then tuned the composition of the Zr-base halide SEs to 165 further elaborate the relation between amorphization and ionic 166 conduction. A series of  $\text{Li}_{2+2x}\text{ZrCl}_4\text{O}_{1+x}$  SEs (x = 0, 0.25, 0.5, 1670.75, and 1) was synthesized from various stoichiometric ratios 168 of ZrCl<sub>4</sub> and Li<sub>2</sub>O. Figure 2a shows the SXRD patterns. The 169 f2 detailed quantification of the phase compositions for each 170  $\text{Li}_{2+2x}\text{ZrCl}_4\text{O}_{1+x}$  SE was obtained by refinement (Figure S6), 171 and the results are summarized in Figure S7. Increasing the 172 ratio of Li<sub>2</sub>O reduced the formation probability of crystalline 173 hcp-Li<sub>2</sub>ZrCl<sub>6</sub>. Minimal impurities of hcp-Li<sub>2</sub>ZrCl<sub>6</sub>, Li<sub>2</sub>O, and 174 LiCl were achieved for  $\text{Li}_{2+2x}\text{ZrCl}_4\text{O}_{1+x}$  when x=0.5, showing 175 the highest degree of amorphization (89.5%) with a further 176 improved O substitution of 42.9% comparing to Li<sub>2</sub>ZrCl<sub>4</sub>O 177 (33.3% of O substitution). EELS mapping for the highly 178 amorphous Li<sub>3</sub>ZrCl<sub>4</sub>O<sub>1.5</sub> sample suggested that the homoge- 179 neous dispersion of Zr, Cl, O, and Li elements constitutes the 180 amorphous component (Figure S8). It is noted that such weak 181

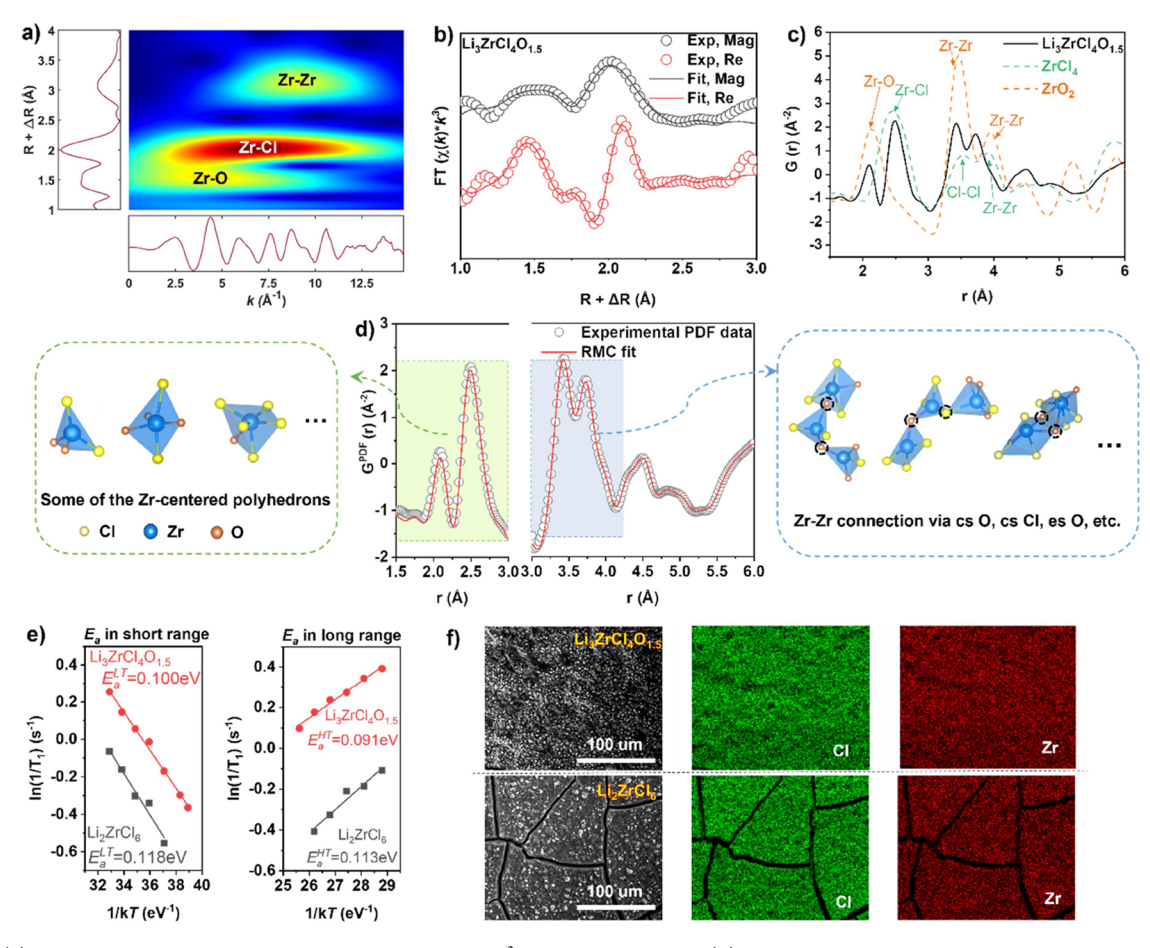


Figure 3. (a) WT spectrum of  $\text{Li}_3\text{ZrCl}_4\text{O}_{1.5}$  at the Zr K-edge. A  $k^3$  weighting was used. (b) FT-EXAFS fitting results for the Zr K-edge spectrum of the  $\text{Li}_3\text{ZrCl}_4\text{O}_{1.5}$  showing the experimental data (gray circle) and Feff modeling (gray line) in terms of magnitude of FT and the real part of FT experimental data (red circle) and Feff modeling (red line) traces. (c) Comparison of the PDFs of  $\text{Li}_3\text{ZrCl}_4\text{O}_{1.5}$ , ZrCl<sub>4</sub>, and ZrO<sub>2</sub>. (d) RMC fit (red line) to the experimental G(r) (gray circle) of  $\text{Li}_3\text{ZrCl}_4\text{O}_{1.5}$ . Several possible basic building blocks in  $\text{Li}_3\text{ZrCl}_4\text{O}_{1.5}$  are shown on the left side. On the right side, the schemes show the connectivity that leads to the edge-sharing and corner-sharing Zr-centered polyhedra in  $\text{Li}_3\text{ZrCl}_4\text{O}_{1.5}$ , respectively. (e) Temperature-dependent <sup>7</sup>Li SLR NMR rates for  $\text{Li}_3\text{ZrCl}_4\text{O}_{1.5}$  and  $\text{Li}_2\text{ZrCl}_6$  measured in the laboratory frame of the reference. (f) Backscattered electron (BSE) images and the corresponding energy dispersive X-ray spectroscopy (EDS) elemental mapping for the surface of cold-pressed  $\text{Li}_3\text{ZrCl}_4\text{O}_{1.5}$  and  $\text{Li}_2\text{ZrCl}_6$  pellets, respectively.

182 crystalline impurity signals in Li<sub>3</sub>ZrCl<sub>4</sub>O<sub>1.5</sub> SEs were even 183 undetectable by lab-based XRD measurements. Further 184 increasing the amount of Li<sub>2</sub>O (x = 0.75 and 1) led to 185 considerable impurities of LiCl and Li<sub>2</sub>O in addition to the 186 amorphous main phases. At the Li/Zr molar ratio of 3:1, and 187 improving the content of Cl or O, neither Cl-rich nor O-rich 188 attempts could show similarly high amorphization as the 189 Li<sub>3</sub>ZrCl<sub>4</sub>O<sub>1.5</sub> (Figure S9).

Ionic conductivities of the  $Li_{2+2x}ZrCl_4O_{1+x}$  SEs (x = 0, 0.25,190 191 0.5, 0.75, and 1) were evaluated via electrochemical impedance spectroscopy measurements. The temperature-dependent 193 Nyquist plots are displayed in Figure S10, and the extracted 194 ionic conductivity values at 25 °C are shown in Figure 2b. The 195 Li<sub>3</sub>ZrCl<sub>4</sub>O<sub>1.5</sub> SE with the highest amorphization showed the <sub>196</sub> highest ionic conductivity of  $(1.35 \pm 0.07) \times 10^{-3}$  S cm<sup>-1</sup> (at 197 25 °C). Arrhenius plots of Li<sub>2+2x</sub>ZrCl<sub>4</sub>O<sub>1+x</sub> samples were compared in Figure 2c. Li<sub>3</sub>ZrCl<sub>4</sub>O<sub>1,5</sub> showed the lowest 199 activation energy  $(E_a)$  of 0.294  $\pm$  0.003 eV. The trend of the 200 activation energies implied that the structures of amorphous proportion showed a flattened energy landscape for Li-ion 202 migration. Additionally, the electronic conductivity of the 203 representative Li<sub>3</sub>ZrCl<sub>4</sub>O<sub>1.5</sub> SE was determined as low as 7.10 204 × 10<sup>-10</sup> S cm<sup>-1</sup> through direct current (DC) polarization

m easurem ents(Figure S11). The value was 7 orders of 205 magnitude lower than that of the ionic conductivity, satisfying 206 the essential requirement of electron insulation for a qualified 207 SE. In addition, compared to the  $\rm Li_2ZrCl_6$  SE (5.61  $\times$  10<sup>-9</sup> S 208 cm<sup>-1</sup>), the highly am orphous  $\rm Li_3ZrCl_4O_{1.5}$  SE shows a lower 209 electronic conductivity, which was also reported previously for 210 the sulfide glass ceramic SE comparing to its highly c rystalline 211 one. 35

To describe the local structure of the amorphous Zr-based 213 halide SEs, we employed X-ray absorption near edge structure 214 (XANES) spectroscopy. Zr K-edge XANES 215 spectra of the SEs were obtained to correlate the average local 216 chemistry with Li-ion migration in the amorphous proportion 217 because

the line shape of the K-edge of a transition metal is  $_{218}$  influenced by the nearest interatomic distances of n eighboring  $_{219}$  atoms. Figure S12 compares the spectral features of  $Li_2ZrCl_6$   $_{220}$  and  $Li_2ZrCl_4O$  along with reference spectra of  $ZrCl_4$  and  $ZrO_2$   $_{221}$  with known structures. The whiteline of  $Li_2ZrCl_6$  showed three  $_{222}$  obvious splits, which were almost identical with the whiteline  $_{223}$  shape for  $ZrCl_4$ . Therefore, the noncrystalline structure in  $_{224}$   $Li_2ZrCl_6$  could be regarded as the fragmented hcp- $Li_2ZrCl_6$   $_{225}$  with three kinds of distinct bond lengths (>0.18 Å between  $_{226}$  each other). In contrast, the whiteline shape of  $Li_2ZrCl_4O$  was  $_{227}$ 

228 smooth and merged, indicating that the differences of bond 229 lengths in Zr-Cl/O polyhedrons became subtle for the O-230 substituted sample. Figure 2d compares the Zr K-edge spectra 231 of  $\text{Li}_{2+2x}\text{ZrCl}_4\text{O}_{1+x}$  SEs (x = 0, 0.5, and 1). With x increasing, 232 the whiteline shape of the spectra changes to be more 233 concentrated without any obvious splits. This further indicates 234 that the nearest Zr-related bond lengths in amorphous 235 Li<sub>2+2x</sub>ZrCl<sub>4</sub>O<sub>1+x</sub> materials are regular and uniform. Zr K-edge 236 FT-EXAFS spectroscopy was then adopted to quantitatively 237 understand the coordination environment around the central 238 Zr in  $\text{Li}_{2+2x}\text{ZrCl}_4\text{O}_{1+x}$  SEs (x = 0, 0.5, and 1) (Figure 2e). 239 Based on the single scattering information from ZrO2 and 240 ZrCl<sub>4</sub> (Figure S4), the peaks resulting from the O and Cl 241 scatters around Zr can be roughly determined, which showed 242 an intensity growth in Zr-O while a decrease in Zr-Cl. This 243 suggests that increasing the x value in Li<sub>2+2x</sub>ZrCl<sub>4</sub>O<sub>1+x</sub> materials 244 led to the replacement of more Cl anions nearest Zr cations by 245 O anions. Consequently, there is a high possibility that 246 displaced Cl anions combine with Li cations to form LiCl 247 impurity, which is consistent with the SXRD results.

In-depth structural analysis was further conducted on the <sup>249</sup> representative  $\text{Li}_3\text{ZrCl}_4\text{O}_{1.5}$  SE. As shown in Figure 3a, phase-<sup>250</sup> uncorrected WT-EXAFS<sup>37,38</sup> confirmed that Zr was succes-251 sively coordinated by O, Cl, and Zr at ~1.5, 2, and 3 Å, 252 respectively. EXAFS fitting (Figure 3b) provides average 253 coordination information nearest to Zr in Li<sub>3</sub>ZrCl<sub>4</sub>O<sub>1.5</sub>. A 254 centered-Zr is surrounded by 2.5 oxygens at 2.07 Å and 5.6 255 chlorines at 2.49 Å (Table S2). RMC modeling for total 256 scattering data was utilized to understand the structure 257 configurations in the most amorphous Li<sub>3</sub>ZrCl<sub>4</sub>O<sub>1.5</sub> SE. As 258 suggested in the PDF profiles in Figure 3c, the first two peaks 259 correspond to Zr-O and Zr-Cl pairs, while the next two 260 peaks within 3.0-4.1 Å are attributed to Zr-Zr bonding. We 261 carried out RMC modeling on both the normalized F(Q) and  $_{262}$   $G^{PDF}(r)$  of Li<sub>3</sub>ZrCl<sub>4</sub>O<sub>1.5</sub> to produce a statistical ensemble 263 reconciling configurations (Figure S13a). The fitted data were 264 in good agreement with the experimental data in both long-265 range orders and local structures (Figure S13b,c). As illustrated 266 in Figure 3d, extracted statistical information around Zr atoms 267 reveals basic building blocks, including  $[ZrO_aCl_b]^{(2a+b-4)-}$  (0  $\leq$  $268 \ b/a < 6$ ) and  $[ZrCl_6]^{2-}$  polyhedrons (Figure S13d). These Zr-269 centered polyhedrons are predominantly connected via corner-270 sharing (cs) Cl ( $\sim$ 55%) and cs O ( $\sim$ 37%), with the rest exhibiting edge-sharing and a few face-sharing configurations (Figure S13e). Over 90% of Cl anions are closely surrounded 273 by Li ions (53%) or served as terminal Cl (38%) (Figure S13f). 274 We further performed 50 repeated RMC runs on Li<sub>3</sub>ZrCl<sub>4</sub>O<sub>1.5</sub> total scattering data, each with distinctive randomness. The 276 small uncertainty for each of the relevant results guarantees the 277 reliability of the RMC resulted conclusion.

The  $E_a$  for Li-ion transport in the determined local 279 structures in Li<sub>3</sub>ZrCl<sub>4</sub>O<sub>1.5</sub> was evaluated by temperature-280 dependent <sup>7</sup>Li spin—lattice relaxation (SLR) nuclear magnetic 281 resonance (NMR) measurements. According to the "Bloem-282 bergen, Purcell and Pound" model, <sup>39</sup> slopes of two-flank 283 divisional points below the highest value of  $1/T_1$  can be used 284 to depict the  $E_a$  of Li-ion migrations in short-range (low-285 temperature flank,  $E_a^{LT}$ ) and long-range (high-temperature 286 flank,  $E_a^{HT}$ ), respectively. <sup>40</sup> As shown in Figure 3e,  $E_a^{LT}$  for 287 Li<sub>3</sub>ZrCl<sub>4</sub>O<sub>1.5</sub> was 0.100 eV, which was around 20% lower than 288 that of Li<sub>2</sub>ZrCl<sub>6</sub> (0.118 eV) with the crystalline phase 289 dominating. The O/Cl corner-sharing Zr-based polyhedral

networks also led to a low  $E_a$  for long-range Li-ion transport 290  $(E_a^{\rm HT}=0.091~{\rm eV})$  in Li<sub>3</sub>ZrCl<sub>4</sub>O<sub>1.5</sub>.

Based on the above structural analyses for the Zr-based 292 halide SEs and corresponding ionic conduction properties, we 293 can claim several important conclusions. First, the amorphous 294 component in the Zr-based halides (synthesized via the one- 295 step BM method) shows a close correlation with the Li-ion 296 conduction behaviors. Second, enhancing the amorphization 297 (or reducing the crystalline impurities) by changing the local 298 structure in the Zr-based halide SEs can improve the ionic 299 conductivity. Third, we demonstrate that the O substitution is 300 effective to facilitate the amorphization of Zr-based halide SEs. 301 Specifically, compared to Li<sub>2</sub>ZrCl<sub>6</sub>, Li<sub>2</sub>ZrCl<sub>4</sub>O shows disor- 302 dered and distorted Zr-O/Cl polyhedrons, in which the bond 303 length of Zr-X (X = Cl, O) is averaged to flatten the energy 304 landscape for Li-ion migration. Furthermore, optimizing the 305 amorphization of Zr-based halide SEs with a higher O content 306 (Li<sub>3</sub>ZrCl<sub>4</sub>O<sub>1.5</sub>) leads to the formation of corner-shared 307 connections within Zr-Zr polyhedrons. These are predom- 308 inances to induce a wide range of distortions of Li sites and 309 lower the energy barriers for Li-ion migration. 41 So far, we 310 have revealed several important factors to cause an improved 311 ionic conduction in amorphous O-substituted Zr-based halide 312 SEs. Among these scenarios, the elongation of the average 313 bond length of Zr-Cl was also theoretically explored by Kwak 314 et al. as one of the main reasons for the high interfacial Li-ion 315 conduction in the crystalline O-substituted Zr-based materi- 316 als.<sup>33</sup> Importantly, the amorphization of Zr-based halide SEs 317 with incorporation of O and the resulting improvement in 318 ionic conductivity can extend to other halides based on Ta, 319 Nb, or Hf as the central element adjacent to Zr in the periodic 320 table, as depicted in Figure S14. While for typical halide SEs 321 with a formula of  $Li_3MCl_6$  (where M = Y, Er), the simple 322 introduction of O by replacing LiCl with Li<sub>2</sub>O reactant proves 323 ineffective in achieving amorphization and enhancing ionic 324 conductivity (Figure S15). This limitation may be associated 325 with the intrinsic glass-formation capability of the central metal 326 element.

In addition to the favorable Li-ion conduction property of 328 the highly amorphous Li<sub>3</sub>ZrCl<sub>4</sub>O<sub>1.5</sub> SE, good mechanical 329 deformability is an extra highlight. As displayed in Figure 3f, at 330 low magnification (in the scale of hundreds of micrometers), 331 the cold-pressed Li<sub>2</sub>ZrCl<sub>6</sub> pellet with low amorphization shows 332 evident cracks on the surface. In sharp contrast, the surface of 333 the Li<sub>3</sub>ZrCl<sub>4</sub>O<sub>1.5</sub> pellet was compact and continuous, indicating 334 the high deformability of highly amorphous materials, which 335 was also reported before for Li-Zr-O-Cl SE by Hu et al.<sup>32</sup> 336 and other amorphous SEs.<sup>42</sup> One important benefit derived 337 from the good deformability of amorphous materials is the 338 potential to minimize grain boundaries (GBs).<sup>43</sup> However, the 339 influence of GBs on the delivered ionic conductivity is still 340 elusive for halide-based SEs, because theoretically the GB 341 effect on the ionic conduction in Li<sub>3</sub>InCl<sub>6</sub> was regarded 342 negligible.<sup>44</sup> Detailed studies about the mechanical properties 343 and GBs are unfortunately beyond the scope of this work and 344 will be investigated in our following research.

The application potential of the amorphous Li<sub>3</sub>ZrCl<sub>4</sub>O<sub>1.5</sub> SE 346 was evaluated in ASSBs. The electrochemical stability window 347 (ESW) of the Li<sub>3</sub>ZrCl<sub>4</sub>O<sub>1.5</sub> SE was determined via linear cyclic 348 voltammetry (LSV) measurements, as shown in Figure S16. 349 The high oxidation limit of 4.1 V and reduction limit of 2 V 350 made it possible to integrate different 4 V class cathode 351 materials. The ESW and electrochemical stability of 352

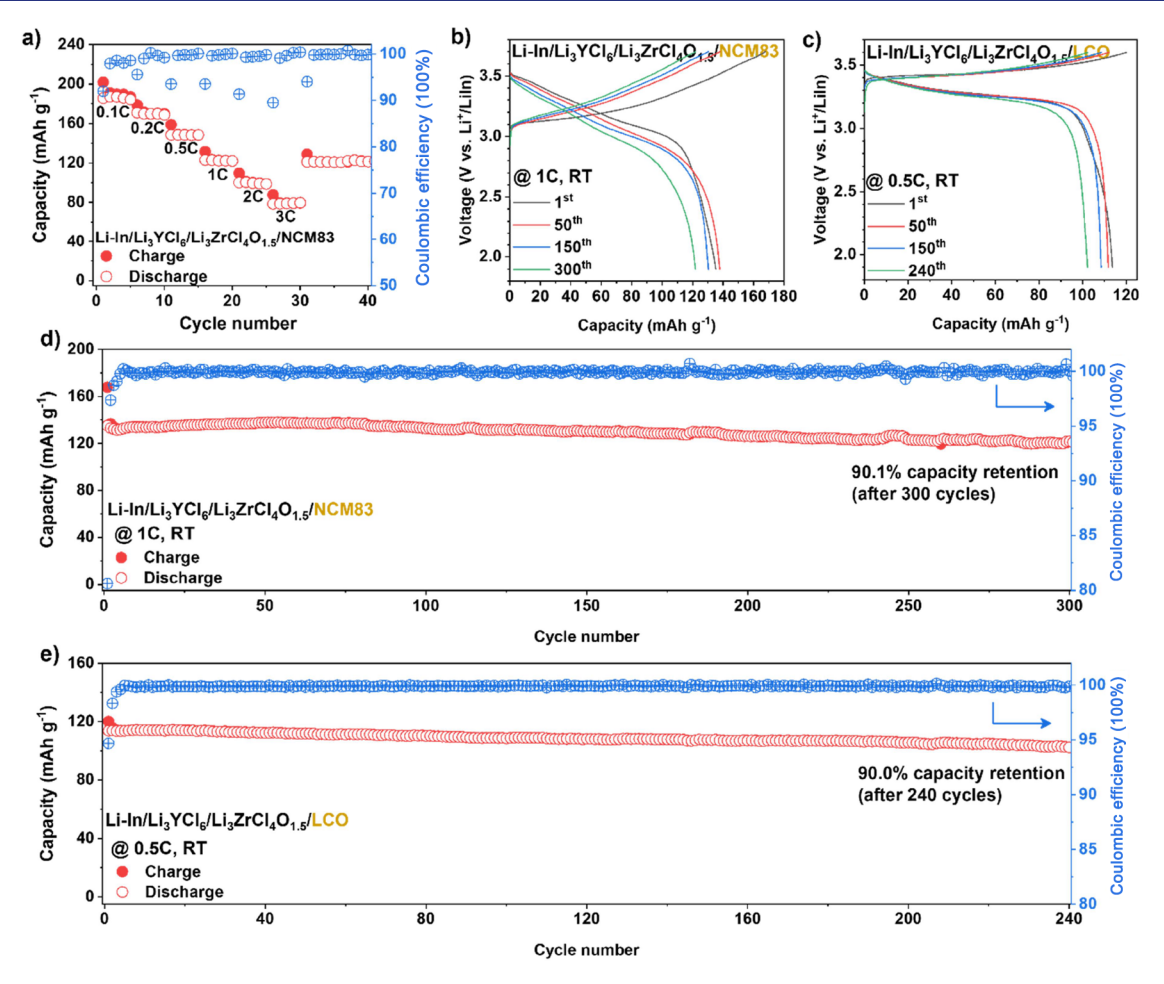


Figure 4. (a) Rate performance of ASSB with the NCM83 cathode at RT. (b) Cycling performance of ASSB with NCM83 cathode and (d) charge—discharge curves at 1 C. (c) Cycling performance of ASSB with LCO cathode and (e) charge—discharge curves at 0.5 C.

353 amorphous Li<sub>3</sub>ZrCl<sub>4</sub>O<sub>1.5</sub> was examined as superior to that of 354 the relatively crystalline Li<sub>2</sub>ZrCl<sub>6</sub> SE. The reason is not only 355 attributed to the benefits of incorporating O<sup>34</sup> and reduced 356 electronic conductivity<sup>35</sup> but also is possibly related to the 357 mechanically constrained effect of the amorphous component in SEs. 45,46 However, considering the high reduction limit of 359 the Li<sub>3</sub>ZrCl<sub>4</sub>O<sub>1.5</sub> SE (2 V), an anode interlayer SE of Li<sub>3</sub>YCl<sub>6</sub> 360 was used to prevent direct contact between Li-In anode and 361 Li<sub>3</sub>ZrCl<sub>4</sub>O<sub>1.5</sub> SEs. 15,18 The electrochemical performance of the constructed ASSBs with high-voltage LiNi<sub>0.83</sub>Co<sub>0.11</sub>Mn<sub>0.06</sub>O<sub>2</sub> 363 (NCM83) was demonstrated. As displayed in Figures 4a and 364 S17a, an excellent rate performance was achieved. The 365 reversible capacities of 185.7, 170.9, 148.4, 123.0, 100.1, and 366 78.5 mAh g<sup>-1</sup> were achieved at 0.1, 0.2, 0.5, 1, 2, and 3 C (1 C  $_{367} = 200 \text{ mA g}^{-1}$ ), respectively. The cycling performance of the 368 NCM83 ASSBs at large current densities was also desirable. As 369 shown in Figure 4b,d, ASSBs could stably operate for over 300 370 cycles with a capacity retention of 90.1% at 1 C. Moreover, a 371 reversible capacity of 96.6 mAh g<sup>-1</sup> could be maintained after 372 ASSB cycling over 600 times at 2 C (Figure S17b). The  $_{\rm 373}$  excellent interfacial compatibility between  $\rm Li_{3}ZrCl_{4}O_{1.5}$  and 374 NCM83 was proved by a close observation on the interfacial 375 composition via cryo-TEM characterizations as displayed in 376 Figure S18, which was in contrast to the interface 377 decomposition between Li<sub>2</sub>ZrCl<sub>6</sub> and NCM83 revealed by 378 Janek and Nazar. 28 That is to say, the incorporation of the O 379 into the Zr-based SEs can prevent the formation of ZrO<sub>2</sub> as the

interfacial reaction product when pairing up with Ni-rich  $_{380}$  cathode materials (e.g., NCM83). Besides the NCM83  $_{381}$  cathode, the LiCoO $_{2}$  (LCO) cathode was also used for the  $_{382}$  Li $_{3}$ ZrCl $_{4}$ O $_{1.5}$  SE-based ASSBs. As exhibited in Figure 4c, the  $_{383}$  initial Coulombic efficiency of LCO ASSB evaluated at 0.5 C  $_{384}$  (1 C = 140 mA g $^{-1}$ ) reached 94.7, and 90.0% of the initially  $_{385}$  reversible capacity could be sustained after 240 consecutive  $_{386}$  cycles (Figure 4e).

# 3. CONCLUSIONS

In summary, taking the Zr-based halide SEs as an example, we 388 successfully illustrated how the amorphous content correlates 389 with the ionic conductivity of some lithium metal (IV or V) 390 (oxy)halide SEs. The amorphization of Zr-based halides (SEs) 391 can be elaborately tuned by incorporating oxygen, resulting in 392 a content change from 46.0 to 89.5%. As an optimized 393 composition, Li<sub>3</sub>ZrCl<sub>4</sub>O<sub>1.5</sub> was highly amorphous and with a 394 high ionic conductivity of  $(1.35 \pm 0.07) \times 10^{-3} \text{ S cm}^{-1}$  at 25 395 °C. Combining synchrotron-based X-ray absorption spectros- 396 copy analysis and RMC fitting, we reveal the local structure of 397 the amorphous Li<sub>3</sub>ZrCl<sub>4</sub>O<sub>1.5</sub> SE. The distorted Zr-O/Cl <sub>398</sub> polyhedrons with averaged Zr-X (X = O, Cl) bond length 399 constitute the anion framework via a desirable O/Cl corner- 400 sharing manner. This is regarded as the intrinsic reason for the 401 promising ionic conductivity. In addition to the improved ionic 402 conductivity, amorphization brings about an enhanced 403 mechanical property. Consequently, the representative 404

496

405 Li<sub>3</sub>ZrCl<sub>4</sub>O<sub>1.5</sub> SEs enable ASSBs operating with outstanding 406 performance at 25 °C. This study shall provide new 407 understandings and design principles of high-performance 408 halide SEs, leading to a key advancement for halide-based 409 ASSBs.

#### 410 ASSOCIATED CONTENT

# 411 Supporting Information

414

415

416

417

418

419

420

421

422

423

424

425

426

427

412 The Supporting Information is available free of charge at 413 https://pubs.acs.org/doi/10.1021/jacs.3c07343.

Experimental section; SXRD ( $\lambda = 0.41 \text{ Å}$ ) pattern of the Li<sub>2</sub>ZrCl<sub>6</sub> prepared; quantification of the amorphous content; cryo-TEM characterizations on the Li2ZrCl4O sample; Zr K-edge wavelet transformed (WT) extended X-ray absorption fine structure (EXAFS) contour plots; Nyquist plots and Arrhenius plots; refinement for the SXRD data; summary of the quantification of the phase composition; cryo-TEM characterizations on the most amorphous Li3ZrCl4O1.5 sample; lab-based XRD patterns; normalized Nyquist plots; DC polarization curves; Zr K-edge XANES spectra; RMC modeling results; extended studies; LSV results; charge-discharge curves; HRTEM image; and structural parameters; references (PDF)

### AUTHOR INFORMATION

#### 429 Corresponding Authors

M. Danny Gu - Eastern Institute for Advanced Study, Eastern 430 Institute of Technology, Ningbo, Zhejiang 315200, P. R. 431 China; Email: m.danny.gu@gmail.com 432

Yuanpeng Zhang - Neutron Scattering Division, Oak Ridge 433 National Laboratory, Oak Ridge, Tennessee 37831, United 434 States; orcid.org/0000-0003-4224-3361; 435

Email: zhangy3@ornl.gov 436

Graham King - Canadian Light Source Inc., Saskatoon, SK 437 S7N 2 V3, Canada; o orcid.org/0000-0003-1886-7254; 438 Email: graham.king@lightsource.ca 439

**Xueliang Sun** – Department of Mechanical and Materials 440 Engineering, Western University, London, ON N6A 5B9, 441 Canada; Eastern Institute for Advanced Study, Eastern 442 443 Institute of Technology, Ningbo, Zhejiang 315200, P. R. China; orcid.org/0000-0003-0374-1245; 444

Email: xsun9@uwo.ca

#### 446 Authors

445

461

462

Shumin Zhang – Department of Mechanical and Materials 447 Engineering, Western University, London, ON N6A 5B9, 448 Canada 449

Feipeng Zhao - Department of Mechanical and Materials 450 Engineering, Western University, London, ON N6A 5B9, 451 Canada 452

Lo-Yueh Chang - National Synchrotron Radiation Research 453 Centre, Hsinchu 30076, Taiwan 454

**Yu-Chun Chuang** — National Synchrotron Radiation Research 455 Centre, Hsinchu 30076, Taiwan; o orcid.org/0000-0002-456 2879-5381 457

**Zhen Zhang** – Department of Materials Science and 458 Engineering, Southern University of Science and Technology, 459 Shenzhen 518055, P. R. China 460

Yuanming Zhu - Research Institute of Interdisciplinary Science and School of Materials Science and Engineering,

```
Dongguan University of Technology, Dongguan 523808,
                                                             463
    China
                                                             464
  Xiaoge Hao - Department of Mechanical and Materials
                                                             465
    Engineering, Western University, London, ON N6A 5B9,
                                                             466
    Canada
                                                             467
  Jiamin Fu - Department of Mechanical and Materials
                                                             468
    Engineering, Western University, London, ON N6A 5B9,
                                                             469
    Canada; Department of Chemistry, Western University,
                                                             470
    London, ON N6A 5B7, Canada
                                                             471
  Jiatang Chen – Department of Chemistry, Western University, 472
    London, ON N6A 5B7, Canada; o orcid.org/0000-0002- 473
    9705-6523
                                                             474
  Jing Luo - Department of Mechanical and Materials
                                                             475
    Engineering, Western University, London, ON N6A 5B9,
                                                             476
    Canada
                                                             477
  Minsi Li - Department of Mechanical and Materials
                                                             478
    Engineering, Western University, London, ON N6A 5B9,
                                                             479
    Canada
                                                             480
  Yingjie Gao - Department of Mechanical and Materials
                                                             481
    Engineering, Western University, London, ON N6A 5B9,
                                                             482
    Canada; o orcid.org/0000-0002-6853-7870
                                                             483
  Yining Huang – Department of Chemistry, Western
                                                             484
    University, London, ON N6A 5B7, Canada; orcid.org/
    0000-0001-9265-5896
                                                             486
  Tsun-Kong Sham - Department of Chemistry, Western
                                                             487
    University, London, ON N6A 5B7, Canada; o orcid.org/
                                                             488
    0000-0003-1928-6697
                                                             489
Complete contact information is available at:
                                                             490
https://pubs.acs.org/10.1021/jacs.3c07343
                                                             491
Author Contributions
                                                             492
                                                             493
                                                             494
                                                             495
```

◆S.Z. and F.Z. contributed equally to this work.

The authors declare no competing financial interest.

# ACKNOWLEDGMENTS

This research was supported by the Natural Sciences and 497 Engineering Research Council of Canada (NSERC), the 498 Canada Research Chair Program (CRC), the Canada 499 Foundation for Innovation (CFI), the Ontario Research 500 Foundation (ORF), and the University of Western Ontario 501 (UWO). The synchrotron research was performed at the 502 Canadian Light Source, a national research facility of the 503 University of Saskatchewan, which was supported by the CFI, 504 NSERC, the National Research Council (NRC), the Canadian 505 Institutes of Health Research (CIHR), the Government of 506 Saskatchewan, and the University of Saskatchewan. Authors 507 thank Sandamini H. Alahakoon from the University of Western 508 Ontario for the assistance of NMR data collection.

# REFERENCES

(1) Xiao, J.; Shi, F. F.; Glossmann, T.; Burnett, C.; Liu, Z. From 511 laboratory innovations to materials manufacturing for lithium-based 512 batteries. Nat. Energy 2023, 8 (4), 329-339.

(2) Grey, C. P.; Hall, D. S. Prospects for lithium-ion batteries and 514 beyond-a 2030 vision. Nat. Commun. 2020, 11 (1), 6279. 515

(3) Zeng, X. Q.; Li, M.; Abd El-Hady, D.; Alshitari, W.; Al-Bogami, 516 A. S.; Lu, J.; Amine, K. Commercialization of Lithium Battery 517 Technologies for Electric Vehicles. Adv. Energy Mater. 2019, 9 (27), 518 No. 1900161. 519

(4) Janek, J.; Zeier, W. G. Challenges in speeding up solid-state 520 battery development. Nat. Energy 2023, 8, 230-240.

- 522 (5) Zhao, Q.; Stalin, S.; Zhao, C.-Z.; Archer, L. A. Designing solid-523 state electrolytes for safe, energy-dense batteries. *Nat. Rev. Mater.* 524 **2020**, 5 (3), 229–252.
- 525 (6) Chen, R.; Li, Q.; Yu, X.; Chen, L.; Li, H. Approaching practically 526 accessible solid-state batteries: stability issues related to solid 527 electrolytes and interfaces. *Chem. Rev.* **2020**, *120* (14), 6820–6877.
- 528 (7) Xia, W.; Zhao, Y.; Zhao, F. P.; Adair, K. G.; Zhao, R.; Li, S.; Zou, 529 R. Q.; Zhao, Y. S.; Sun, X. L. Antiperovskite Electrolytes for Solid-530 State Batteries. *Chem. Rev.* **2022**, *122* (3), 3763–3819.
- 531 (8) Feng, X. Y.; Fang, H.; Wu, N.; Liu, P. C.; Jena, P.; Nanda, J.; 532 Mitlin, D. Review of modification strategies in emerging inorganic 533 solid-state electrolytes for lithium, sodium, and potassium batteries. 534 *Joule* **2022**, *6* (3), 543–587.
- 535 (9) Wu, J. H.; Liu, S. F.; Han, F. D.; Yao, X. Y.; Wang, C. S. 536 Lithium/Sulfide All-Solid-State Batteries using Sulfide Electrolytes. 537 Adv. Mater. 2021, 33 (6), No. 2000751.
- 538 (10) Liang, J. W.; Li, X. N.; Adair, K. R.; Sun, X. L. Metal halide 539 superionic conductors for all-solid-state batteries. *Acc. Chem. Res.* 540 **2021**, 54 (4), 1023–1033.
- 541 (11) Li, X. N.; Liang, J. W.; Yang, X. F.; Adair, K. R.; Wang, C. H.; 542 Zhao, F. P.; Sun, X. L. Progress and perspectives on halide lithium 543 conductors for all-solid-state lithium batteries. *Energy Environ. Sci.* 544 **2020**, 13 (5), 1429–1461.
- 545 (12) Wang, C.; Liang, J.; Kim, J. T.; Sun, X. Prospects of halide-546 based all-solid-state batteries: From material design to practical 547 application. *Sci. Adv.* **2022**, *8* (36), No. eadc9516.
- 548 (13) Kwak, H.; Wang, S.; Park, J.; Liu, Y. S.; Kim, K. T.; Choi, Y.; 549 Mo, Y. F.; Jung, Y. S. Emerging Halide Superionic Conductors for All-550 Solid-State Batteries: Design, Synthesis, and Practical Applications. 551 ACS Energy Lett. 2022, 7 (5), 1776–1805.
- 552 (14) Tanaka, Y.; Ueno, K.; Mizuno, K.; Takeuchi, K.; Asano, T.; 553 Sakai, A. New Oxyhalide Solid Electrolytes with High Lithium Ionic 554 Conductivity > 10 mS/cm for All-Solid-State Batteries. *Angew. Chem.*, 555 *Int. Ed.* **2023**, *62* (13), No. e202217581.
- 556 (15) Asano, T.; Sakai, A.; Ouchi, S.; Sakaida, M.; Miyazaki, A.; 557 Hasegawa, S. Solid halide electrolytes with high lithium-ion 558 conductivity for application in 4 V class bulk-type all-solid-state 559 batteries. *Adv. Mater.* **2018**, 30 (44), No. 1803075.
- 560 (16) Li, X. N.; Liang, J. W.; Luo, J.; Banis, M. N.; Wang, C. H.; Li, 561 W. H.; Deng, S. X.; Yu, C.; Zhao, F. P.; Hu, Y. F.; Sham, T. K.; Zhang, 562 L.; Zhao, S. Q.; Lu, S. G.; Huang, H.; Li, R. Y.; Adair, K. R.; Sun, X. L. 563 Air-stable Li3InCl6 electrolyte with high voltage compatibility for all-564 solid-state batteries. *Energy Environ. Sci.* **2019**, *12* (9), 2665–2671.
- 565 (17) Liang, J. W.; Li, X. N.; Wang, S.; Adair, K. R.; Li, W. H.; Zhao, 566 Y.; Wang, C. H.; Hu, Y. F.; Zhang, L.; Zhao, S. Q.; Lu, S. G.; Huang, 567 H.; Li, R. Y.; Mo, Y. F.; Sun, X. L. Site-occupation-tuned superionic 568 Li<sub>(x)</sub>ScCl<sub>(3+x)</sub> halide solid electrolytes for all-solid-state batteries. *J. Am.* 569 *Chem. Soc.* **2020**, *142* (15), 7012–7022.
- 570 (18) Zhou, L.; Zuo, T.-T.; Kwok, C. Y.; Kim, S. Y.; Assoud, A.; 571 Zhang, Q.; Janek, J.; Nazar, L. F. High areal capacity, long cycle life 4 572 V ceramic all-solid-state Li-ion batteries enabled by chloride solid 573 electrolytes. *Nat. Energy* **2022**, *7*, 83–93.
- 574 (19) Fu, J. M.; Wang, S.; Liang, J. W.; Alahakoon, S. H.; Wu, D. J.; 575 Luo, J.; Duan, H.; Zhang, S. M.; Zhao, F. P.; Li, W. H.; Li, M. S.; Hao, 576 X. G.; Li, X. A.; Chen, J. T.; Chen, N.; King, G.; Chang, L. Y.; Li, R. 577 Y.; Huang, Y. N.; Gu, M.; Sham, T. K.; Mo, Y. F.; Sun, X. L. 578 Superionic Conducting Halide Frameworks Enabled by Interface-579 Bonded Halides. J. Am. Chem. Soc. 2023, 145 (4), 2183–2194.
- 580 (20) Yin, Y.-C.; Yang, J.-T.; Luo, J.-D.; Lu, G.-X.; Huang, Z.; Wang, 581 J.-P.; Li, P.; Li, F.; Wu, Y.-C.; Tian, T.; Meng, Y.-F.; Mo, H.-S.; Song, 582 Y.-H.; Yang, J.-N.; Feng, L.-Z.; Ma, T.; Wen, W.; Gong, K.; Wang, L.-583 J.; Ju, H.-X.; Xiao, Y.; Li, Z.; Tao, X.; Yao, H.-B. A LaCl3-based 584 lithium superionic conductor compatible with lithium metal. *Nature* 585 **2023**, 616 (7955), 77–83.
- 586 (21) Li, X. N.; Liang, J. W.; Chen, N.; Luo, J.; Adair, K. R.; Wang, C. 587 H.; Banis, M. N.; Sham, T. K.; Zhang, L.; Zhao, S. Q.; Lu, S. G.; 588 Huang, H.; Li, R. Y.; Sun, X. L. Water-Mediated Synthesis of a 589 Superionic Halide Solid Electrolyte. *Angew. Chem., Int. Ed.* **2019**, 58 590 (46), 16427–16432.

- (22) Zhou, L. D.; Kwok, C. Y.; Shyamsunder, A.; Zhang, Q.; Wu, X. 591 H.; Nazar, L. F. A new halospinel superionic conductor for high- 592 voltage all solid state lithium batteries. *Energy Environ. Sci.* **2020**, *13* 593 (7), 2056–2063.
- (23) Schlem, R.; Muy, S.; Prinz, N.; Banik, A.; Shao-Horn, Y.; Zobel, 595 M.; Zeier, W. G. Mechanochemical Synthesis: A Tool to Tune Cation 596 Site Disorder and Ionic Transport Properties of Li3MCl6 (M = Y, Er) 597 Superionic Conductors. *Adv. Energy Mater.* **2020**, *10* (6), 598 No. 1903719.
- (24) Kwak, H.; Han, D.; Lyoo, J.; Park, J.; Jung, S. H.; Han, Y.; 600 Kwon, G.; Kim, H.; Hong, S. T.; Nam, K. W.; Jung, Y. S. New Cost-601 Effective Halide Solid Electrolytes for All-Solid-State Batteries: 602 Mechanochemically Prepared Fe3+-Substituted Li2ZrCl6. Adv. Energy 603 Mater. 2021, 11 (12), No. 2003190.
- (25) Wang, K.; Ren, Q. Y.; Gu, Z. Q.; Duan, C. M.; Wang, J. Z.; 605 Zhu, F.; Fu, Y. Y.; Hao, J. P.; Zhu, J. F.; He, L. H.; Wang, C. W.; Lu, 606 Y. Y.; Ma, J.; Ma, C. A cost-effective and humidity-tolerant chloride 607 solid electrolyte for lithium batteries. *Nat. Commun.* 2021, 12 (1), 608 4410.
- (26) Schlem, R.; Banik, A.; Ohno, S.; Suard, E.; Zeier, W. G. Insights 610 into the Lithium Sub-structure of Superionic Conductors Li3YCl6 611 and Li3YBr6. *Chem. Mater.* **2021**, 33 (1), 327–337.
- (27) Sebti, E.; Evans, H. A.; Chen, H. N.; Richardson, P. M.; White, 613 K. M.; Giovine, R.; Koirala, K. P.; Xu, Y. B.; Gonzalez-Correa, E.; 614 Wang, C. M.; Brown, C. M.; Cheetham, A. K.; Canepa, P.; Clement, 615 R. J. Stacking Faults Assist Lithium-Ion Conduction in a Halide-Based 616 Superionic Conductor. J. Am. Chem. Soc. 2022, 144 (13), 5795–5811. 617
- (28) Kochetkov, I.; Zuo, T. T.; Ruess, R.; Singh, B.; Zhou, L. D.; 618 Kaup, K.; Janek, J.; Nazar, L. Different interfacial reactivity of lithium 619 metal chloride electrolytes with high voltage cathodes determines 620 solid-state battery performance. *Energy Environ. Sci.* **2022**, *15* (9), 621 3933–3944.
- (29) Ishiguro, Y.; Ueno, K.; Nishimura, S.; Iida, G.; Igarashib, Y. 623 TaCl5-glassified Ultrafast Lithium Ion-conductive Halide Electrolytes 624 for High-performance All-solid-state Lithium Batteries. *Chem. Lett.* 625 **2023**, 52 (4), 237–241.
- (30) Zhang, S.; Zhao, F.; Chen, J.; Fu, J.; Luo, J.; Alahakoon, S. H.; 627 Chang, L.-Y.; Feng, R.; Shakouri, M.; Liang, J.; Zhao, Y.; Li, X.; He, 628 L.; Huang, Y.; Sham, T.-K.; Sun, X. A family of oxychloride 629 amorphous solid electrolytes for long-cycling all-solid-state lithium 630 batteries. *Nat. Commun.* 2023, 14 (1), 3780.
- (31) Hayashi, A.; Hama, S.; Morimoto, H.; Tatsumisago, M.; 632 Minami, T. Preparation of Li2S-P2S5 amorphous solid electrolytes by 633 mechanical milling. *J. Am. Ceram. Soc.* **2001**, 84 (2), 477–479.
- (32) Hu, L.; Wang, J.; Wang, K.; Gu, Z.; Xi, Z.; Li, H.; Chen, F.; 635 Wang, Y.; Li, Z.; Ma, C. A cost-effective, ionically conductive and 636 compressible oxychloride solid-state electrolyte for stable all-solid-637 state lithium-based batteries. *Nat. Commun.* 2023, 14 (1), 3807.
- (33) Kwak, H.; Kim, J.-S.; Han, D.; Kim, J. S.; Park, J.; Kwon, G.; 639 Bak, S.-M.; Heo, U.; Park, C.; Lee, H.-W.; Nam, K.-W.; Seo, D.-H.; 640 Jung, Y. S. Boosting the interfacial superionic conduction of halide 641 solid electrolytes for all-solid-state batteries. *Nat. Commun.* 2023, 14 642 (1), 2459.
- (34) Li, B.; Li, Y.; Zhang, H.-S.; Wu, T.-T.; Guo, S.; Cao, A.-M. Fast 644 Li+-conducting Zr4+-based oxychloride electrolyte with good thermal 645 and solvent stability. *Sci. China Mater.* **2023**, 66 (8), 3123–3128.
- (35) Wang, S.; Zhang, W. B.; Chen, X.; Das, D.; Ruess, R.; Gautam, 647 A.; Walther, F.; Ohno, S.; Koerver, R.; Zhang, Q.; Zeier, W. G.; 648 Richter, F. H.; Nan, C. W.; Janek, J. Influence of Crystallinity of 649 Lithium Thiophosphate Solid Electrolytes on the Performance of 650 Solid-State Batteries. Adv. Energy Mater. 2021, 11 (24), No. 2100654. 651
- (36) Natoli, C. R. *EXAFS and Near Edge Structure III.* In Proceedings 652 of an International Conference, Stanford, CA, July 16–20; Hodgson, 653 K. O.; Hedman, B.; Penner-Hahn, J. E., Eds.; Springer Berlin, 654 Heidelberg: Stanford, CA, 1984; pp. 38–42.
- (37) Xia, Z. M.; Zhang, H.; Shen, K. C.; Qu, Y. Q.; Jiang, Z. Wavelet 656 analysis of extended X-ray absorption fine structure data: Theory, 657 application. *Physica B* **2018**, 542, 12–19.

- 659 (38) Munoz, M.; Argoul, P.; Farges, F. Continuous Cauchy wavelet 660 transform analyses of EXAFS spectra: A qualitative approach. *Am.* 661 *Mineral.* **2003**, 88 (4), 694–700.
- 662 (39) Bloembergen, N.; Purcell, E. M.; Pound, R. V. Relaxation 663 Effects in Nuclear Magnetic Resonance Absorption. *Phys. Rev.* **1948**, 664 73 (7), 679–712.
- 665 (40) Yu, C.; Ganapathy, S.; de Klerk, N. J. J.; Roslon, I.; van Eck, E. 666 R. H.; Kentgens, A. P. M.; Wagemaker, M. Unravelling Li-Ion
- 667 Transport from Picoseconds to Seconds: Bulk versus Interfaces in an
- 668 Argyrodite Li6PSSCl—Li2S All-Solid-State Li-Ion Battery. *J. Am.*
- 669 Chem. Soc. 2016, 138 (35), 11192-11201.
- 670 (41) Jun, K.; Sun, Y.; Xiao, Y.; Zeng, Y.; Kim, R.; Kim, H.; Miara, L. 671 J.; Im, D.; Wang, Y.; Ceder, G. Lithium superionic conductors with 672 corner-sharing frameworks. *Nat. Mater.* **2022**, *21*, 924–931.
- 673 (42) Chi, X. W.; Zhan, Y.; Hao, F.; Kmiec, S.; Dong, H.; Xu, R.;
- 674 Zhao, K. J.; Ai, Q.; Terlier, T.; Wang, L.; Zhao, L. H.; Guo, L. Q.;
- 675 Lou, J.; Xin, H. L.; Martin, S. W.; Yao, Y. An electrochemically stable 676 homogeneous glassy electrolyte formed at room temperature for all-
- 676 homogeneous glassy electrolyte formed at room temperature for all 677 solid-state sodium batteries. *Nat. Commun.* **2022**, 13 (1), 2854.
- 678 (43) Milan, E.; Pasta, M. The role of grain boundaries in solid-state 679 Li-metal batteries. *Mater. Futures* **2023**, 2 (1), No. 013501.
- 680 (44) Quirk, J. A.; Dawson, J. A. Design Principles for Grain 681 Boundaries in Solid-State Lithium-Ion Conductors. *Adv. Energy Mater.* 682 **2023**, *13* (32), No. 2301114.
- 683 (45) Fitzhugh, W.; Ye, L. H.; Li, X. The effects of mechanical 684 constriction on the operation of sulfide based solid-state batteries. *J.* 685 *Mater. Chem. A* **2019**, *7* (41), 23604–23627.
- 686 (46) Wu, F.; Fitzhugh, W.; Ye, L. H.; Ning, J. X.; Li, X. Advanced 687 sulfide solid electrolyte by core-shell structural design. *Nat. Commun.* 688 **2018**, 9 (1), 4037.